Tectonophysics 694 (2017) 424–435

Contents lists available at ScienceDirect

Tectonophysics

journal homepage: www.elsevier.com/locate/tecto

# Detailed microseismicity study in the area of Florina (Greece): Evidence for fluid driven seismicity

Maria Mesimeri [a,*], Vassilios Karakostas [a], Eleftheria Papadimitriou [a], George Tsaklidis [b], Theodoros Tsapanos [a]

[a] Geophysics Department, School of Geology, Aristotle University of Thessaloniki, GR54124 Thessaloniki, Greece
[b] Department of Statistics and Operational Research, School of Mathematics, Aristotle University of Thessaloniki, GR54124 Thessaloniki, Greece

ARTICLE INFO

*Article history:*
Received 8 June 2016
Received in revised form 7 October 2016
Accepted 15 November 2016
Available online 16 November 2016

*Keywords:*
Microseismicity
Waveform cross correlation
Crustal model
Fluid intrusion
Repeating events
$CO_2$ emissions

ABSTRACT

A local seismic network was installed and operated in the area of Florina, northern Greece, during July 2013 – January 2014 for studying the high microseismic activity following the occurrence of an $M_w = 4.1$ event on 17 February 2013. The recordings of the local network along with the ones of the Hellenic Unified Seismological Network (HUSN) are used for obtaining accurate locations and defining the characteristics of the seismic activity. A new velocity model is calculated for a broader area using the recordings of the HUSN stations. Relocation is performed for 1330 events recorded by the local network and 423 events recorded by HUSN using the double difference technique and cross correlation measurements. Fault plane solutions are determined for the two largest events ($M_w = 3.6$ and $M_w = 4.1$) using waveform inversion technique. The causative fault of the largest event ($M_w = 4.1$) is striking almost E-W and dipping to the north. However, most of the activity is concentrated in its south and forms an almost vertical, south dipping plane, striking almost E-W. This southern cluster consists of multiplets and is located in an area of positive Coulomb stress changes, due to the coseismic slip of the $M_w = 4.1$ earthquake. The spatio-temporal evolution of microseismicity is in most cases well explained by diffusion curves, a signature of fluid induced seismicity. However, there are cases where a triggering front could not describe the evolution of the activity resulting to an earthquake - earthquake triggering. The dependent or independent (Poisson process) earthquake occurrence was examined by searching their interevent time distribution. These characteristics are interpreted as the consequence of $CO_2$ emission through faults which are used as pathways in an area enhanced by the coseismic Coulomb stress changes.



## 1. Introduction

Microseismicity studies conducted by the deployment of temporal local networks contribute to a better understanding of the underlying mechanism of seismogenesis. Imaging of major faults along with identification of smaller ones could be achieved through this procedure. This line of research is followed for the Florina Basin (Fig. 1) located in Northwestern Greece. It consists an intermountain graben composed of metamorphic rocks and formed as a result of extensional stress following the Alpine orogenesis (Koukouzas et al., 2015 and references therein). Historical and instrumental catalogs include only five earthquakes with $5.0 \le M \le 6.0$ (Papazachos and Papazachou, 2003) in the broader area of northwestern Greece (stars in Fig. 1). The largest one, which occurred in 1709 ($M = 6.0$) about 20 km south of Florina, caused light damage to few temples of this city. Three earthquakes with $M = 5.4$ occurred in epicentral distances from 20 to 30 km north of Florina in 1920, 1958 and 1994, respectively. There is one more earthquake occurred in 1984 with $M = 5.2$ at a distance of 40 km ESE of Florina.

In 2012 an increase in the seismic activity was observed in the western part of the area near Lake Prespa forming two small clusters (blue circles in Fig. 1). In the meantime, activity started near Florina with the largest earthquake ($M_w = 4.1$) on 17 February 2013. In the following months seismic activity was continued with a big number of low magnitude earthquakes. The detectability of the Hellenic Unified Seismological Network (HUSN) (hexagons in Fig. 1 inset map) is not adequate to efficiently record the microseismicity. Therefore, six seismological stations were installed in the area (triangles in Fig. 1) and their recordings were used in combination with the ones of HUSN.

The area is well known for carbonate rich springs and $CO_2$-rich gas vents, which are used for commercial purposes, and observed throughout the Florina Basin (squares in Fig. 1). Springs are most probably produced by a slow upwelling of magmatic, hydrothermal $CO_2$ across faults (Hatziyannis, 2007; Ziogou et al., 2013). Koukouzas et al. (2015) assumed that NE-SW oriented faults are acting as fluid flow pathways, allowing for localized leakage at the surface. The authors also pointed out that the migration of $CO_2$ gases could range from few hundred

* Corresponding author.
*E-mail addresses:* mmesimer@geo.auth.gr (M. Mesimeri), vkarak@geo.auth.gr (V. Karakostas), ritsa@geo.auth.gr (E. Papadimitriou), tsaklidi@math.auth.gr (G. Tsaklidis), tsapanos@geo.auth.gr (T. Tsapanos).

http://dx.doi.org/10.1016/j.tecto.2016.11.027
0040-1951/

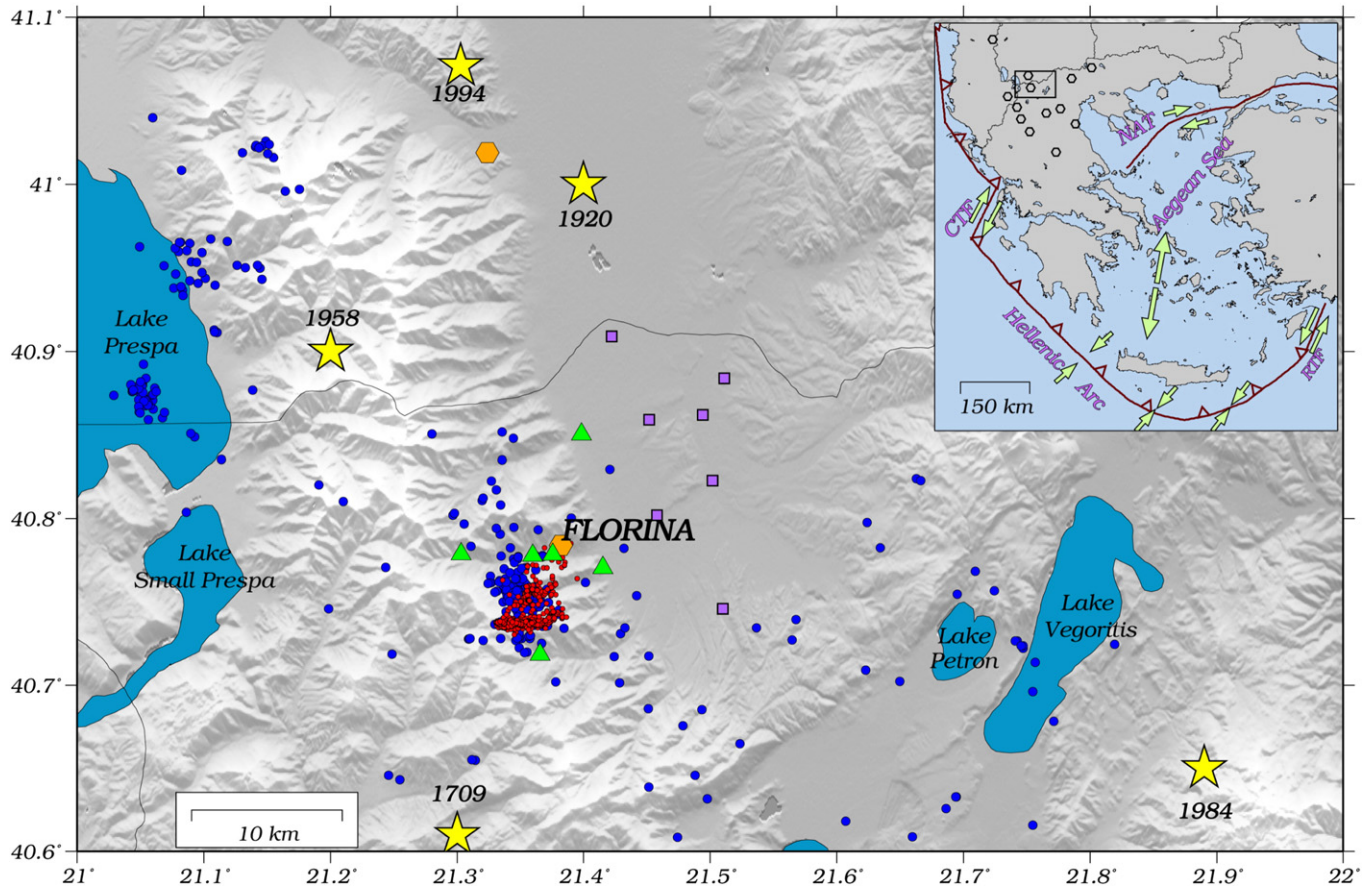


**Fig. 1.** Morphological map of northwestern Greece along with the relocated epicenters of earthquakes recorded by the permanent network that occurred during 2012–2014 January (blue circles) and these by the temporal network during July 2013–January 2014 (red circles). The earthquakes with M ≥ 5 (both historical and instrumental) are depicted by stars. With squares are shown the major $CO_2$ springs of commercial use. Hexagons show the HUSN seismological stations and triangles the stations of the local network. Inset map. The back-arc Aegean and the surrounding area, with the dominant seismotectonic features: Hellenic Arc, North Aegean Trough (NAT), the Cephalonia (CTF) and Rhodes (RTF) Transform Faults. The study area is enclosed in the rectangle. Hexagons show the HUSN seismological stations.

meters to kilometers before they finally arrive to the surface. Similar patterns were observed in other intra-continental regions such as West Bohemia and Vogtland (e.g. Fischer et al., 2014 and references therein), where in most cases epicenter distribution overlaps roughly with the occurrence of gas escapes. Another example is in northern Italy, where the Colfiorito aftershock sequence was initiated by a high pressure $CO_2$ source at depth (Miller et al., 2004). Several studies were conducted using experimental data in order to define the governing mechanisms of this kind of microseismicity (e.g. Mayr et al., 2011; Stanchits et al., 2011). In areas of high microseismicity, the induced activity due to fluid intrusion is usually described by diffusion curves (e.g. Shapiro et al., 1997, 2002; Hainzl, 2004; Hainzl et al., 2012; Parotidis et al., 2003, 2004, 2005; Shelly et al., 2013).

The aim of the present study is to examine the temporal and spatial evolution of the microseismicity, and to identify the triggering mechanism and any possible relation with $CO_2$ emission. In respect to that, a new crustal model was determined combining data from both local and permanent networks. Earthquake catalogs were compiled using the recordings of both networks, and high accuracy was achieved after applying waveform cross correlation and double difference technique. Possible triggering mechanisms are considered such as Coulomb stress changes and fluid diffusion for interpreting the seismicity evolution. The detailed microseismicity analysis in combination with local geological observations by other studies, contributes to the understanding of the underlying triggering mechanism.

## 2. Data analysis

Data from both the regional and the temporal local networks were used for the purposes of the present study. We gathered all the available recordings of 13 broadband digital stations of HUSN, which is in operation since 2008 and covers adequately the area of Greece, located at epicentral distances <150 km (hexagons in Fig. 1 inset map) from Florina, with sampling rate of digitization 100 samples/s. Phases of 521 earthquakes that occurred during 2012–2013 were collected from the monthly bulletins of the Geophysics Department of Aristotle University of Thessaloniki and the National Observatory of Athens (NOA).

The local seismic network was installed at the end of July 2013 and operated until the end of January 2014. It consisted of 6 stations equipped with three component broadband seismometers (Guralp CMG40T) and high resolution (24 bits) digitizers (Reftek 130-01) with sampling rate 125 samples/s (triangles in Fig. 1). Time and station location were accurately evaluated by GPS receivers. Approximately 1500 earthquakes, with at least 4 P- and 3 S- phases, were detected after visual inspection of the waveforms with P- and S- phases manually picked.

### 2.1. Relocation process

The two datasets were analyzed separately, following the same procedure. Firstly, the Wadati method was applied to the permanent and to the local network datasets and the $V_p/V_s$ ratio was found to be equal to

1.790 and 1.807, respectively. A proper velocity model, which is required for accurate earthquake location, is not available for the area, although several models (e.g. Hatzfeld et al., 1987, 1997; Drakatos et al., 2005) were proposed for the broader northern Greece after the deployment of local networks or using earthquakes recorded by the permanent network. In this study a new velocity model is obtained using the VELEST software (Kissling et al., 1994) and the earthquakes with 4 or more P- phases recorded by the permanent network. VELEST does not automatically adjust layer thickness and for that reason an a-priori velocity model consisting of layers with 1 km thickness is used. The inversion was repeated several times using a damping coefficient of 0.01 for the station delays and 0.1 for the velocity model. A new updated a-priori 1D model with corresponding station residuals was obtained and used for locating all earthquakes recorded by HUSN with the HYPOINVERSE program (Klein, 2002). The procedure was repeated with VELEST using a damping coefficient of 0.1 for the station delays and 1.0 for the velocity model. Finally, the layers where differences in velocity were <0.05 km/s, were merged and a new crustal model was obtained (Table 1) along with station delays.

The estimated P-wave velocity model consists of four layers over a half space at a depth of 16 km, with velocities varying between 5.45 and 6.43 km/s. Given that the stations are in distances smaller than 150 km, a velocity for $P_n$ waves was not resolved. Thus, the lower layer was constrained up to a depth of 31 km, and the half space velocity was taken equal to 7.9 km/s (Panagiotopoulos and Papazachos, 1985). The new crustal model and the HYPOINVERSE software (Klein, 2002) were used for the earthquake locations of both datasets. Time delays were calculated for these stations following a procedure described by Karakostas et al. (2014).

The method described by Schaff et al. (2004) and Schaff and Waldhauser (2005) was followed for computing differential times from waveform cross correlation. The two datasets were cross correlated separately in order to obtain differential times different for each one. A time domain correlation function was applied to 60 s waveforms available for each event for both networks. The waveforms were band-pass filtered (2–10 Hz) and updated for P- and S- picked phases when available. Different window lengths were used for the waveforms of the permanent and the local network, respectively. Longer window lengths, which give lower residuals and forming sharper foci locations (Schaff et al., 2004), are preferable in regions of sparse network and low seismicity (e.g. Papadimitriou et al., 2016). On the other hand, when the network is dense close to the seismic activity, resulting to small S - P differences, shorter windows are necessary (e.g. Valoroso et al., 2013). In the present study, 2 s window lengths around P- and S- arrivals with a ±1 s lag search were chosen for the permanent network. Event pairs with correlation coefficient (CC) larger than 70% were kept, which consist of ~19,000 P- and 17,000 S- phases. For the local network, the recorded events have a mean value of S - P equal to 1 s and a mean epicentral distance of 5.5 km. After testing several windows, we chose a window of 0.6 s for both P- and S- arrivals. Because of the manual picking of the phases and the density of the network, the lag search was set equal to ±0.1 s. Event pairs with CC ≥ 80% and 3P or 6S observations were kept resulting to ~40,000 P- and ~150,000 S-phases.

The double difference algorithm *hypoDD* (Waldhauser and Ellsworth, 2000; Waldhauser, 2001) was used to relocate the events. Cross correlation differential times and travel-time differences for P- and S- picked phases were jointly inverted for each network separately in order to obtain highly accurate locations. Due to the large amount of data, all the calculations in the *hypoDD* application were performed using the conjugate gradients method (LSQR) as proposed by Paige and Saunders (1982). For the permanent network ~14,000 P- and ~8000 S-phases were added from catalog data and fifteen iterations were performed in three sets. For the local network ~40,000 P- and ~40,000 S-phases were added from catalog data and thirteen iterations were performed in two sets. In the first five iterations the cross-correlation data were down-weighted by a factor of 100 to allow location from the catalog data in both datasets. For the remaining iterations, eight for the local network and ten for the permanent, the catalog data were down-weighted by a factor of 100 in order to allow cross-correlation to define small structures. The final catalog, available on the website: http://geophysics.geo.auth.gr/ss/station_index_en.html, includes 423 earthquakes recorded by the permanent network with mean root mean square (RMS) 0.010 s and a mean horizontal and vertical errors approximately ~35 m, and 1330 earthquakes from the local network with mean RMS 0.002 s and a mean horizontal and vertical error equal to 1–2 m.

**Table 1**
Estimated 1D velocity model.

| Velocity (km/s) | Depth (km) |
|---|---|
| 5.45 | 0.00 |
| 5.55 | 1.00 |
| 6.20 | 9.00 |
| 6.30 | 13.00 |
| 6.43 | 16.00 |
| 7.90 | 31.00 |

### 2.2. Magnitude estimation

Magnitude estimation of the local events was performed with spectral analysis of all the available recordings using the vertical component waveforms (P-waves). Initially, the instrument responses were removed and a window of ±0.6 s, before and after P- arrival was selected. By integration, data were converted to displacement and Fast Fourier Transform was applied. Each spectrum was corrected for attenuation and the low frequency level $\Omega_o$ was determined as the mean value of $\Omega(f)$ for frequencies 1–10 Hz. Then, the seismic moment was calculated following the model proposed by Brune (1970)

$$M_o = \frac{\Omega_0 4\pi\rho v^3 r}{\Re_{\Theta,\varphi} F} \quad (1)$$

where $\rho = 2750$ kg/m$^3$ is the density of the medium, $v$ is the P wave velocity ($v = 6000$ m/s), $r$ is hypocentral distance (geometrical spreading correction), $\Re_{\Theta,\varphi}$ is radiation pattern correction considered equal to 0.6 (Aki and Richards, 2002) and $F$ is the free surface amplification equal to 2. The mean value of $M_o$ was calculated using all the available stations for each event and moment magnitude was obtained from (Hanks and Kanamori, 1979).

$$M_w = \frac{\log M_o - 16.1}{1.5} \quad (2)$$

For the definition of data completeness, the goodness-of-fit (GFT) method (Wiemer and Wyss, 2000) was applied, by calculating the residuals between the observed frequency magnitude distribution (FMD) of the earthquake catalog and a synthetic distribution which represents a perfect fit to power law for each magnitude bin (Fig. 2). The threshold magnitude ($M_c$) was found equal to 1.3 where the residuals are 4.44% (95.56% GFT). The a- and b-values were estimated using the maximum likelihood method (Aki, 1965) and found equal to 4.11 and 1.01, respectively.

### 2.3. Fault plane solutions determination

Fault plane solutions for the two major events on February 17 ($M_w = 3.6$, $M_w = 4.1$) are available from NOA (Table 2). Their fault plane solutions were also computed in this study using the ISOLA moment tensor inversion package (Sokos and Zahradnik, 2008, 2013). The computed moment tensors showed a fault striking almost E-W and dipping to the north at a dip angle of 50°, similar to the solutions provided by NOA as shown in Table 2. The resulting fault plane solutions

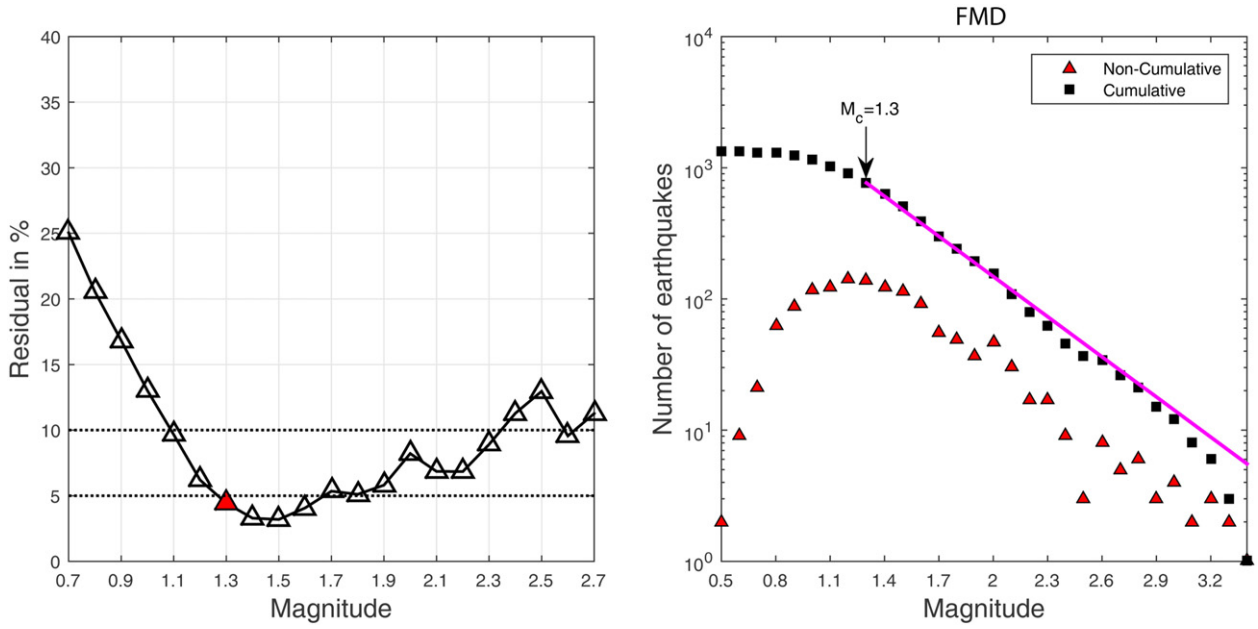


**Fig. 2.** Residual plot between the observed frequency magnitude distribution (FMD) and the perfect fit of the power law for each magnitude bin. Red triangle shows the completeness magnitude ($M_c$) (left). Non-cumulative (triangles) and cumulative (squares) FMD, respectively of the earthquake catalog compiled by the local network (right). The line represents the best fitting model after the application of GFT method.

are in accordance with the NE-SW regional extensional stress regime (Papazachos et al., 1998).

## 3. Seismic activity analysis

The relocated seismicity shown in Fig. 3a reveals a seismic zone mainly divided in two clusters. Blue and red colors were used to denote epicenters recorded by the permanent and the local networks, respectively. Yellow circle and star denote the two largest shocks recorded by the permanent network whereas the size of symbols is proportional to the events magnitudes (Fig. 3b). The denser cluster of earthquakes is located in the southernmost part of the study area (south of 40.74° N), with the vast majority of them being recorded by the local network and aligned in a narrow almost E-W oriented seismic zone. A second cluster including the two largest earthquakes of the sequence is positioned to the north. Although the general trend of the seismic zone is rather N-S, taking into account the orientation of the southern cluster, the local morphology, the regional stress regime and the focal mechanisms of the largest earthquakes, a cross section attempted along the line N-N′ (Fig. 3b), normal to the alignment of the clusters. The hypocentral distribution along this profile defines a seismic zone generally dipping to the north with focal depths ranging from 2 km to 8 km. However, a clear separation between the southern cluster and the rest of the activity is observed.

Seismic activity started in the cluster which includes the largest earthquake at depths ~4.5 km – 6 km (blue symbols in Fig. 3). This cluster with dimensions 2 × 2 km dipping at 45° to the north was considered to be associated with the fault segment which produced the $M_w = 4.1$ earthquake. The length of this seismic zone agrees with a fault corresponding to an $M_w = 4.1$ earthquake derived from scaling laws (Wells and Coppersmith, 1994; Papazachos et al., 2004).

In both the map and the cross section (Fig. 3) a narrow, very well defined south dip zone is shown. It has an almost east - west orientation and almost vertical dipping, with focal depths ranging between 2 km and 4.5 km. All these events were recorded by the local network and are shown with the red symbols in Fig. 3. Low magnitude events were recorded there, with the largest one having a magnitude of $M_w = 3.4$.

### 3.1. Spatio-temporal evolution of microseismic activity

The spatio-temporal evolution of the seismic activity is examined since 29 July 2013 (zero day in Fig. 4) after the installation of the local network. The seismicity rate of the complete catalog ($M_c = 1.3$) shows fluctuations with noticeable quiescence periods (Fig. 4). There are clusters lasting from few hours to several days with low magnitude events (Fig. 4, right axis). The longest quiescence periods occurred between the days 66–78 (04–15 October) and 110–118 (17–24 November) with few low magnitude events ($M_w < 2.0$). During the period of 66–118 days (04 October–24 November) the area was almost quiet with the lowest seismicity rate observed during the monitoring time. Thus, it is assumed that microseismic activity is separated in at least two distinct periods (0–66 day, 118–175 day) during the monitoring time.

Period A starts with small magnitude events (Fig. 4) until the 36th day (03 September) when an event with $M_w = 3.0$ occurred and followed by its own aftershocks. On the 53rd day a second $M_w = 3.1$ event struck the area followed by two events of $M_w = 3.4$ and $M_w = 3.0$ on the 56th (24 September) and 57th (25 September) days. After 52 days

**Table 2**
Fault plane solutions for the two major earthquakes computed in the present study along with the solutions of NOA.

| | Origin time | | Epicenter | | Depth | $M_o$ | $M_w$ | Fault plane solution | | | P–axis | | T–axis | |
|---|---|---|---|---|---|---|---|---|---|---|---|---|---|---|
| Reference | Date | Time | Lon(°E) | Lat(°N) | (km) | (N × m) | | Strike(°) | Dip(°) | Rake(°) | Azimuth | Dip | Azimuth | Dip |
| This study | 17 Feb | 12:06:47 | 21.3298 | 40.7559 | 6.0 | $3.5\ 10^{14}$ | 3.6 | 233 | 50 | −132 | 77 | 59 | 172 | 3 |
| NOA | 17 Feb | 12:06:47 | 21.4037 | 40.7730 | 6.0 | $2.6\ 10^{14}$ | 3.5 | 227 | 54 | −137 | 76 | 54 | 168 | 2 |
| This study | 17 Feb | 16:48:49 | 21.3537 | 40.7512 | 5.0 | $1.8\ 10^{15}$ | 4.1 | 224 | 49 | −124 | 66 | 65 | 158 | 1 |
| NOA | 17 Feb | 16:48:49 | 21.3818 | 40.7862 | 6.0 | $1.4\ 10^{15}$ | 4.0 | 228 | 49 | −122 | 68 | 67 | 160 | 1 |

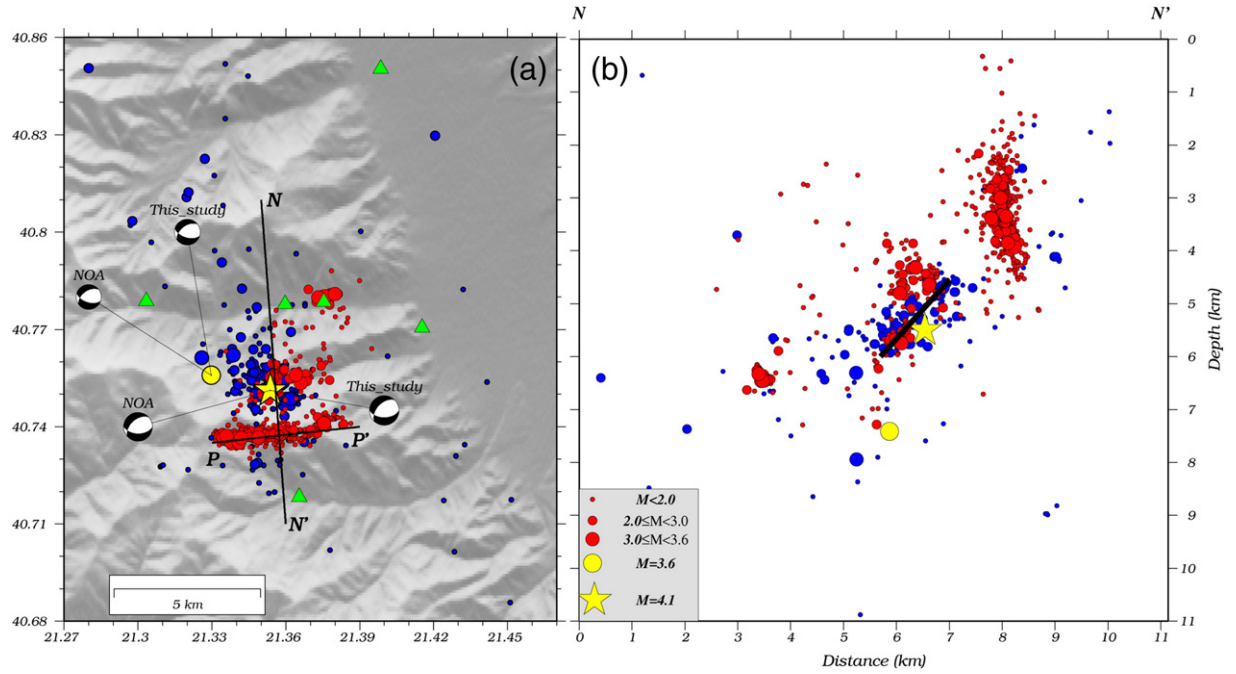


**Fig. 3.** (a) Epicentral distribution of the relocated earthquakes along with fault plane solutions of the two strongest events of the sequence (see Table 2). The locations obtained from recordings of HUSN are depicted with blue circles and with red circles are shown the locations obtained from the local network. N-N′ and P-P′ are normal and parallel to the strike cross sections. P-P′ is shown in Fig. 5 (b) Cross section of the relocated earthquakes along the line of N-N′. Black line denotes the fault associated with the largest event.

of quiescence, period B starts on the 118th day (24 November) with the seismicity rate abruptly increasing. Six earthquakes with M ≥ 3.0 occurred in the first days of period B (118th–125th days; 24 November–01 December) accompanied by a large number of low magnitude events. Later on the 126th day (02 December), seismicity rate again decreased and few smaller clusters occurred until the end of the monitoring time (177th day; 31 January 2014).

The activity was mainly located at the southern part of the area (south of 40.74° N) (Fig. 5a) which was activated repeatedly during the monitoring time. For the first twenty days the activity was comprised inside a ~2.5 km area. Then, the seismicity was migrated almost 1 km in both directions. At the beginning of period B, the entire southern part was activated in a total length of 3 km. Finally, an activity at the westernmost part of the southern cluster started on the 162nd day (January 08) and lasted up to the end of the monitoring. Fig. 5b shows the depth evolution with time for the southern cluster. We observe that all the events are comprised in the shallower layer (2–4 km) with the largest events (stars on Fig. 5b) mostly in deeper parts. It is also worth to note that near the 50th day, after the strongest earthquake (star Fig. 5b), all the following events are in shallower depths forming a leaning plane. The same pattern is also observed after the 118th day (start of period B). These constitute evidence that the fluids in the area migrated to shallower depths in order to meet the surface. Although seismicity occupied the entire area, the persistent activation of the southern part is quite remarkable. For that reason, the properties of this burst will be examined in the following parts.

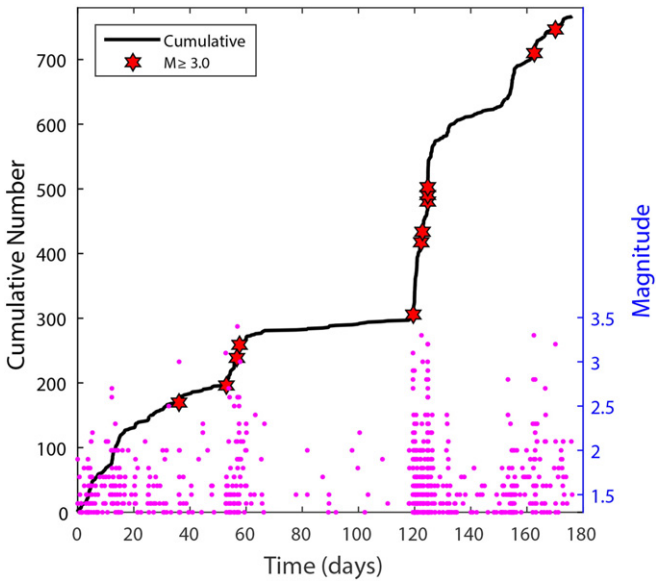


**Fig. 4.** Cumulative number of events (left axis) and magnitude (right axis) against time for the complete catalog ($M_c$ = 1.3). Stars show the earthquakes with $M_w$ ≥ 3.0.

### 3.2. Interevent time distribution

Earthquakes are considered to occur either as independent events, described by the Poisson process, or as triggered by other events described by Omori aftershock law. Interevent time distributions, i.e., times between successive events, were thoroughly examined in order to explain the seismogenesis process in an area and to identify whether the earthquakes occur randomly (following a Poisson process) or are triggered by other events. In case of the Poisson process, the probability distribution for the interevent times would be an Exponential function, whereas in case of triggered events the probability distribution differs from the Exponential one. A power law distribution for the interevent times has been proposed for describing the triggering process (e.g. Bak et al., 2002; Hainzl and Fischer, 2002). Further studies conducted by Corral (2004, 2006) showed that the triggering effect for interevent times could be well described by a Gamma distribution after normalizing the interevent times with seismicity rate. A bimodal distribution for the interevent times, combining Gamma and Exponential distributions was proposed by Touati et al. (2009, 2011), who assumed that events with shorter interevent times are triggered by each other (Gamma distribution) and the longest interevent times indicate independent events (Exponential distribution). Langenbruch et al. (2011) proposed an

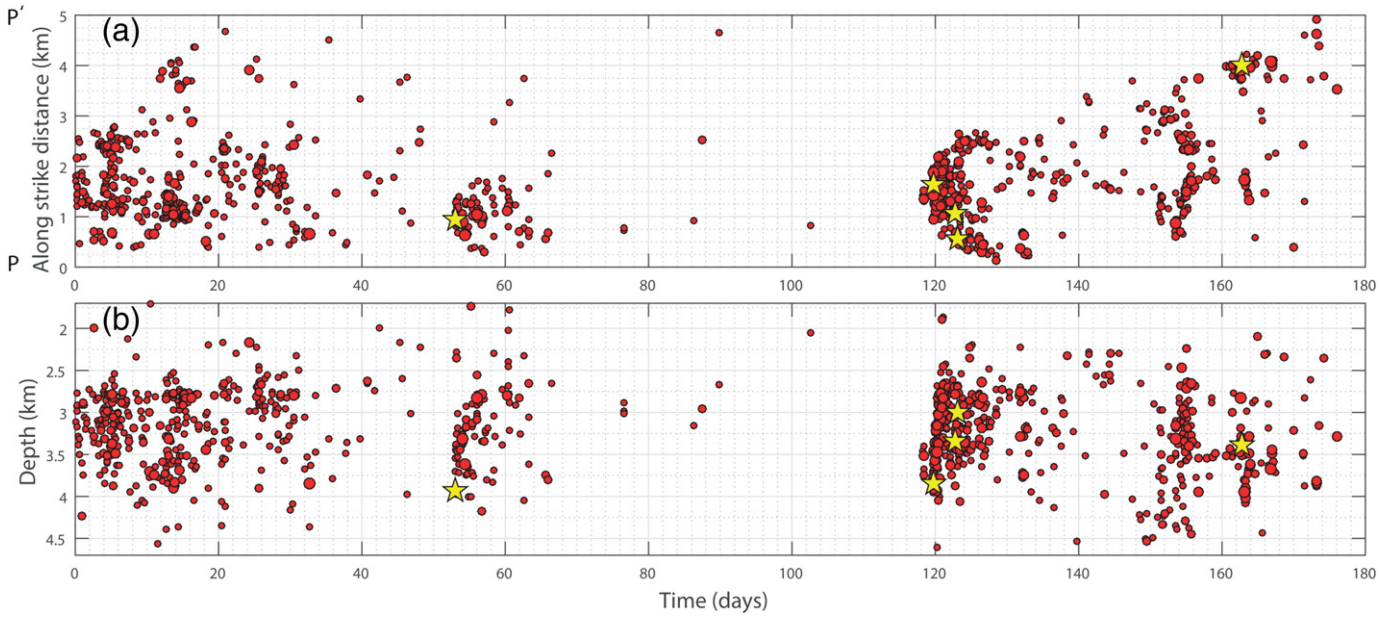


**Fig. 5.** (a) Along strike cross section in West East direction (P-P′ in Fig. 3a) and (b) depth evolution with time of the southern cluster. Stars depict events with $M_w \geq 3.0$.

Exponential distribution for fluid – injection - induced earthquakes resulting to a homogeneous Poisson process, meaning that the events occurred independently. Davidsen and Kwiatek (2013) combined data from different origins (e.g. induced by mining, fluid-injection) and different scales of seismicity. They found that the distribution of interevent times is best fitted by Gamma distribution and is scale and origin independent. Godano (2015) proposed a modified version of the Gamma distribution for interevent times, which takes into account the deviations from the Gamma distribution in shorter interevent times. Considering the above, we focus on the distribution of the interevent times of the southern cluster in order to gain a better understanding of the seismogenesis process.

Corral (2004, 2006) defined probability density as the number of interevent times within a small interval of values, normalized to the total number of interevent times and divided by the length of the small interval. Following this definition, the probability density function was computed for the complete dataset ($M_c = 1.3$) of the southern cluster. The Lognormal, Weibul, Gamma and Exponential distributions were fitted to the observed data (Fig. 6). In order to select the best model, the Kolmogorov-Smirnov (K-S) test was applied to examine the sample fitness for each distribution. Then, the Akaike Information Criterion (AIC) and the Bayesian Information Criterion (BIC) were considered. The estimated parameters are reported in Table 3 for all the examined distributions. The Lognormal distribution describes best the interevent time distribution of the southern cluster, having the lowest values for AIC and BIC and the lowest value of the K-S test. The least fitted distribution is the Exponential one, which is rejected according to the K-S test. Weibull distribution has similar but higher values than the Lognormal distribution. Gamma distribution could not be rejected but the values of AIC, BIC and K-S test show that it is far from the best model. The rejection of the Exponential distribution reveals that seismicity in the area could not be described by the Poisson process. Hence, the fitting of the Lognormal distribution leads to the conclusion that the (consecutive) events are not independent but triggered by each other.

## 4. Triggering mechanisms

### 4.1. Coulomb stress changes

The distribution of the coseismic Coulomb stress changes due to the coseismic slip of the $M_w = 4.1$ earthquake is studied here, aiming to investigate whether the large amount of events of the southern cluster were possibly triggered by this event. This off-fault activity, widely discussed in the literature (e.g. Stein et al., 1994; Stein, 1999; Harris, 1998; Karakostas et al., 2003, 2004), is considered to be the consequence of the stress transfer from the activated fault to its adjacent ones. The change in Coulomb failure function (ΔCFF) depends on both changes in shear stress, $\Delta\tau$, and normal stress, $\Delta\sigma$, and takes the form

$$\Delta CFF = \Delta\tau + \mu(\Delta\sigma + \Delta p) \quad (3)$$

where $\Delta p$ is the pore pressure change, and $\mu$ is the friction coefficient. According to Rice and Cleary (1976), pore pressure is calculated

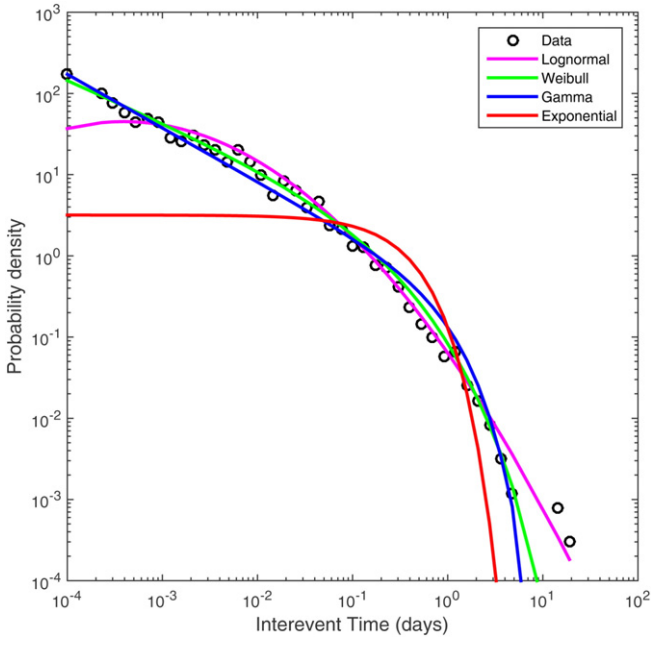


**Fig. 6.** Probability density function for the interevent times of the southern cluster. Different distributions (Lognormal, Weibull, Gamma and Exponential) were fitted to the observed data.

**Table 3**
Estimated parameters and 95% confidence intervals for the different distributions along with Kolmogorov-Smirnov test results (K-S), AIC and BIC criteria. The critical value is equal to 0.214.

| Distribution | Parameters | K-S | *p*-Value | AIC | BIC |
|---|---|---|---|---|---|
| Lognormal | $\mu = -3.15$ [−3.33, −2.97] $\sigma = 2.16$ [2.04, 2.3] | 0.024 | 1.00 | −1052 | −1049 |
| Weibull | a = 0.12 [0.10, 0.14] b = 0.49 [0.46, 0.52] | 0.065 | 0.99 | −1009 | −1006 |
| Gamma | a = 0.33 [0.30, 0.37] b = 0.93 [0.78, 1.10] | 0.147 | 0.32 | −876 | −873 |
| Exponential | $\mu = 0.31$ [0.29, 0.34] | 0.393 | $3.3 \cdot 10^{-6}$ | −168 | −166 |

by the following equation

$$\Delta p = -B\frac{\Delta\sigma_{kk}}{3} \quad (4)$$

where B is the Skempton's coefficient ($0 \le B < 1$) and $\Delta\sigma_{kk}$ expresses summation over the diagonal elements of the stress tensor. We consider a fault plane with 2 km width and 2 km length, according to the aftershock distribution of the largest event (17 February 2013, $M_w = 4.1$), and a dip angle 45°. The average coseismic slip is calculated from the seismic moment computed in the present study (Table 2). We used values of $\mu = 0.75$ and $B = 0.5$ following previous studies (e.g. Robinson and McGinty, 2000; Papadimitriou et al., 2016) and Poisson ratio 0.25. The shear modulus is considered equal to $3.3 \times 10^4$ MPa.

Coulomb stress changes were calculated on a vertical plane, normal to the strike of the ruptured fault (cross section of Fig. 3) according to the faulting type of the southern cluster. The results are depicted in Fig. 7 where bright colors represent regions with positive stress changes and dark colors these with negative ones. The aftershocks of the $M_w = 4.1$ earthquake are plotted with same symbols as in Fig. 3. Earthquakes on the fault plane could not be resolved because a homogeneous slip is assumed. Seismicity burst on the southern cluster is located inside an area of positive stress changes (bright colors) with some events inside lobes with ΔCFF ≥ 0.01 MPa, evidencing triggering by the $M_w = 4.1$ earthquake.

### 4.2. Fluid diffusion

The large number of the low magnitude events of the southern cluster along with its geometry led us to examine any association of this cluster with fluid diffusion. It is known that the spatio-temporal features of hydraulically induced seismicity could be identified in a very natural way from the concept of triggering fronts (Shapiro et al., 1997, 2002). The estimated distance r of the propagating front of significant pore pressure perturbations from the source is described by the equation

$$r = \sqrt{4\pi Dt} \quad (5)$$

where D is the diffusivity and t the elapsed time since the beginning of the fluid intrusion. This equation is valid for a homogeneous and isotropic medium and is used here as a first approximation, assuming that the permeability is constant.

Parotidis et al. (2004) examined the seismicity occurred in areas where fluid injections in boreholes were carried out. They observed that seismicity does not stop immediately but continues after the termination of the injection. Hence, another relation, in addition to the triggering front, is proposed between distance r and occurrence time t in order to explain the continuing activity. Particularly, the authors found that for small distances pore pressure increases rapidly with the injection initiation and stops immediately after its termination. Then for larger distances the pore pressure increases gradually until it takes its

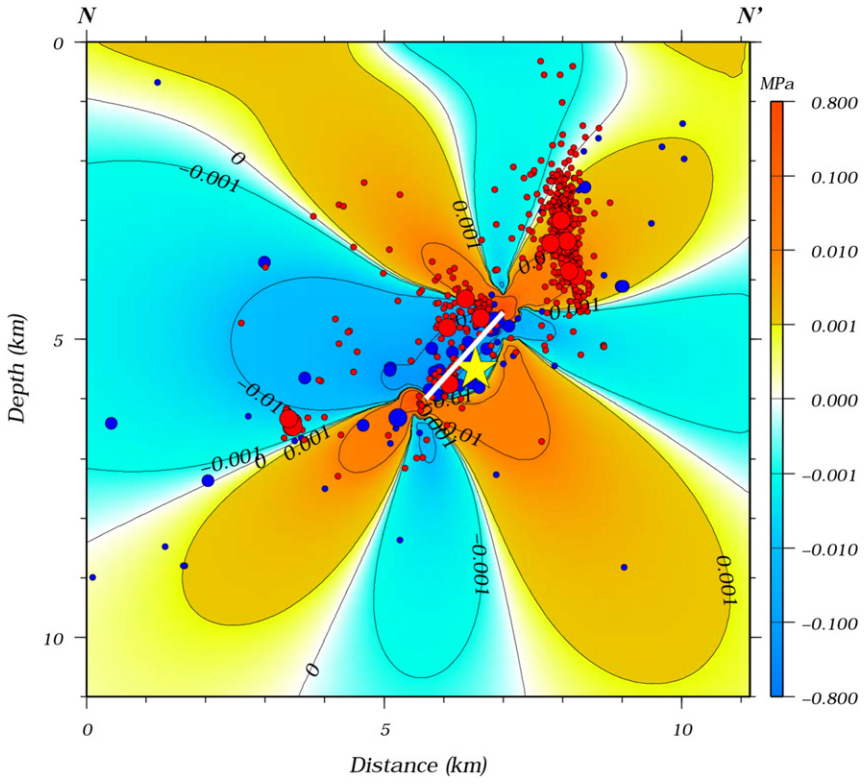


**Fig. 7.** Coulomb stress changes due to the coseismic slip of the major event, 17 February 2013, $M_w = 4.1$, resolved onto a vertical plane in the direction N-N′ (map of Fig. 3). Symbols are the same as in Fig. 3.

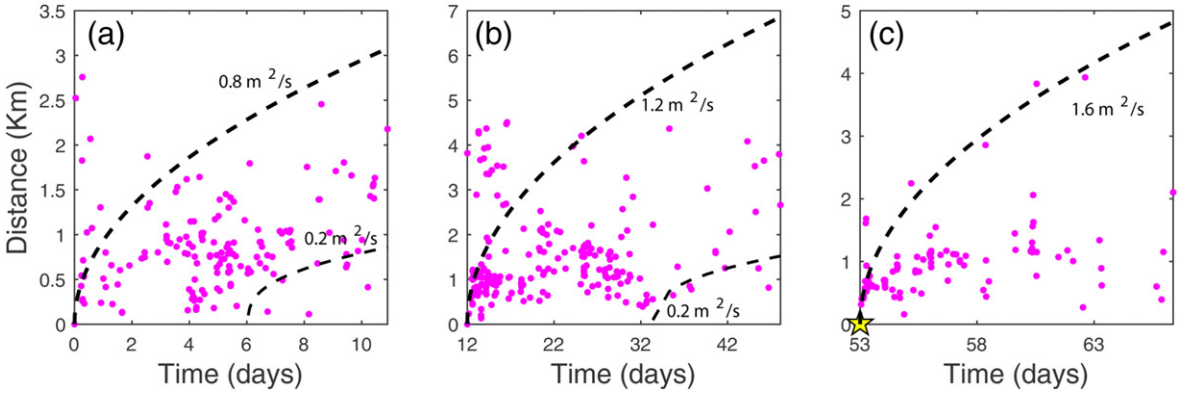


**Fig. 8.** Distance – time (r-t) plots for period A of the local network operation. The envelope curve of the triggering front and the back front is shown by dashed line along with the values of diffusivity. With stars are shown events with $M_w \geq 3.0$. All the events are located in the southern cluster.

maximum value at a certain time $t_1$, larger than time $t_o$, which is the duration of the injection, resulting to occurrence of events after its termination. The above is well described by the parabolic equation

$$r = \sqrt{6Dt\left(\frac{t}{t_0} - 1\right)\ln\left(\frac{t}{t - t_o}\right)} \quad (6)$$

for given diffusivity D, and injection duration $t_o$ defining the back front of induced seismicity. These parabolic like-envelopes (triggering front - back front) of the cloud of events are important signatures of the hydraulically triggered seismicity (Shapiro, 2015).

In case of seismicity studies where there is not an injection point or the possible fluid source is unknown, the first earthquake of the cluster is considered as initial point. In the present study we focus on the two distinct periods of the activity in the southern cluster, applying r – t plots for a constant value of D. Firstly, we examine period A (0–66 days) (Fig. 8) considering the focal coordinates of the first event as zero point. For the first 11 days (Fig. 8a) a parabola with $D = 0.8\ m^2/s$ is well fitted to the observed seismicity and a back front on the 6th day with $D = 0.2\ m^2/s$ describes its termination. From day 12 to 52 the triggering front is fitted with $D = 1.2\ m^2/s$, whereas seismicity seems to stop after the 32nd day (Fig. 8b) and the back-front parabola is fitted with $D = 0.2\ m^2/s$. From 53 to 66 day a parabolic curve is fitted with $D = 1.6\ m^2/s$ (Fig. 8c). This cluster started on the 53rd day with an $M_w = 3.1$ event and expanded to a total 2 km length in the first days, without any evidence for further migration. It is possible that this activity may have the characteristics of a typical mainshock – aftershock sequence.

Period B starts on the 118th day, following the quiescence period, lasting up to the end of the monitoring period. The fit of the parabola curve is examined for the 118–132 days (Fig. 9a) and for the 133–176 days (Fig. 9b). The seismicity starts on the 118th day with small in magnitude events followed by one day of quiescence (Fig. 9a). Then an $M_w = 3.1$ earthquake (first star in Fig. 9a) occurred and triggered several low magnitude earthquakes. Six days after the initiation of period B (124 day) seismicity started decreasing in shorter distances and later in larger distances. This pattern is well explained by the back front equation (Fig. 9a). For the remaining days (133–176) a parabola was fitted with $D = 1.0\ m^2/s$ with no evidence for back front curve (Fig. 9b).

### 4.3. Repeating events

Studies searching for repeating events were conducted on regional (e.g. Schaff and Richards, 2004, 2011) and on local scale (e.g. Waldhauser and Schaff, 2008). Multiplets were observed, i.e., clusters of repeating events, consisting of few earthquakes that were distributed in the entire area, contrary to larger multiplets which are confined at certain areas, probably creeping segments. Aiming to identify particular patches on the rupture fault, we search over for repeating events based on full waveform similarity (P- and S- waves). Cross correlation

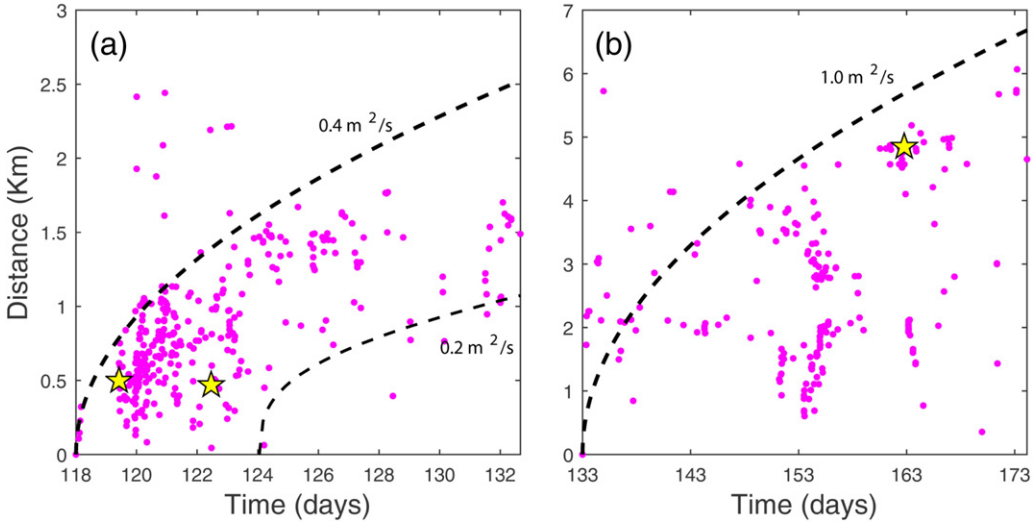


**Fig. 9.** Same as Fig. 8 from the 118th day up to the end of the monitoring period.

**Table 4**
Multiplets of repeating events.

| N of events in multiplet | 2 | 3 | 4 | 5 | 6 | 7 | 9 | 11 | 12 | 27 | 44 | 46 | 661 |
|---|---|---|---|---|---|---|---|---|---|---|---|---|---|
| N of multiplets | 41 | 18 | 8 | 5 | 2 | 3 | 2 | 1 | 1 | 1 | 2 | 1 | 1 |
| Percent (%) | 7.5 | 5.0 | 2.9 | 2.3 | 1.1 | 1.9 | 1.7 | 1.0 | 1.1 | 2.5 | 8.1 | 4.2 | 60.7 |

measurements were applied for 5 s window lengths after P- wave arrival and event pairs with CC ≥ 96% were kept. Following the definition by Got et al. (1994) we consider an event to be part of a multiplet when it is a doublet with at least one other event in the multiplet. 1089 out of 1330 events were identified as members of multiplets (Table 4), which is approximately ~82% of the total seismicity. Almost 86% of the multiplets contain >10 events with the most multitudinous multiplet consists of 661 events. Fig. 10 shows an example of 13 earthquakes included in the second largest multiplet and recorded at station SKOP, which is located ENE of the southern cluster. The plot reveals that earthquakes recorded in this station for the particular multiplet have very similar, almost identical waveforms.

In Fig. 11 the foci of multiplets with >9 events are plotted in a normal cross section (N-N′ in Fig. 3), without considering the multiplet consisting of 11 events which is located outside the study area. The southern cluster seems to be repeatedly activated with five different south dipping multiplets occurred in the area. The largest multiplet contains 661 earthquakes and has the largest dimensions. Four more multiplets consisting of few events have ruptured certain patches on the southern part of the area. One more north dipping multiplet observed in the middle cluster is associated with the structure activated after the $M_w = 4.1$ earthquake. Another small cluster, which occurred to the north and lasted few hours, was identified as a south dipping multiplet. Almost all multiplets are located at the edge of the seismic zone ruptured after the $M_w = 4.1$ earthquake, revealing that a similar mechanism is responsible for earthquake triggering in the area.

## 5. Discussion - conclusions

The $M_w = 4.1$ earthquake occurred near the city of Florina on 17 February 2013 is associated with a north dipping structure, according to spatial distribution of relocated seismicity and the fault plane solutions computed in this study. In order to monitor the progression of several months microseismicity, a local temporal network was installed at the end of July 2013, for the first time in the area. During six months of monitoring about 1500 events were detected with 1330 of them being located with high accuracy. It is noteworthy that during 2012–2013 only 521 earthquakes were detected by the permanent network in the broader area of northwestern Greece, almost three times less than the earthquakes detected by the local network in its six months operation. Microseismicity, particularly during the operation of the local network, is mainly distributed in the southern part of the activated area. This activation was not noticed earlier by the recordings of the permanent network. The focal depths of the events comprised in the southern cluster revealed an almost vertical distribution, in contrast to the structure correlated with the main event, which is north dipping and located at larger depths.

Spatial and temporal evolution of the southern cluster reveals two distinct periods (A – B) during the monitoring period lasting 66 and 56 days, respectively. The main activity is concentrated in the southern part of the area, where small clusters were triggered repeatedly. An important characteristic of this activity is the time-depth evolution of the earthquakes. It is shown that earthquakes started in deeper parts (~4 km) and then migrated to shallower depths (up to ~2 km). This

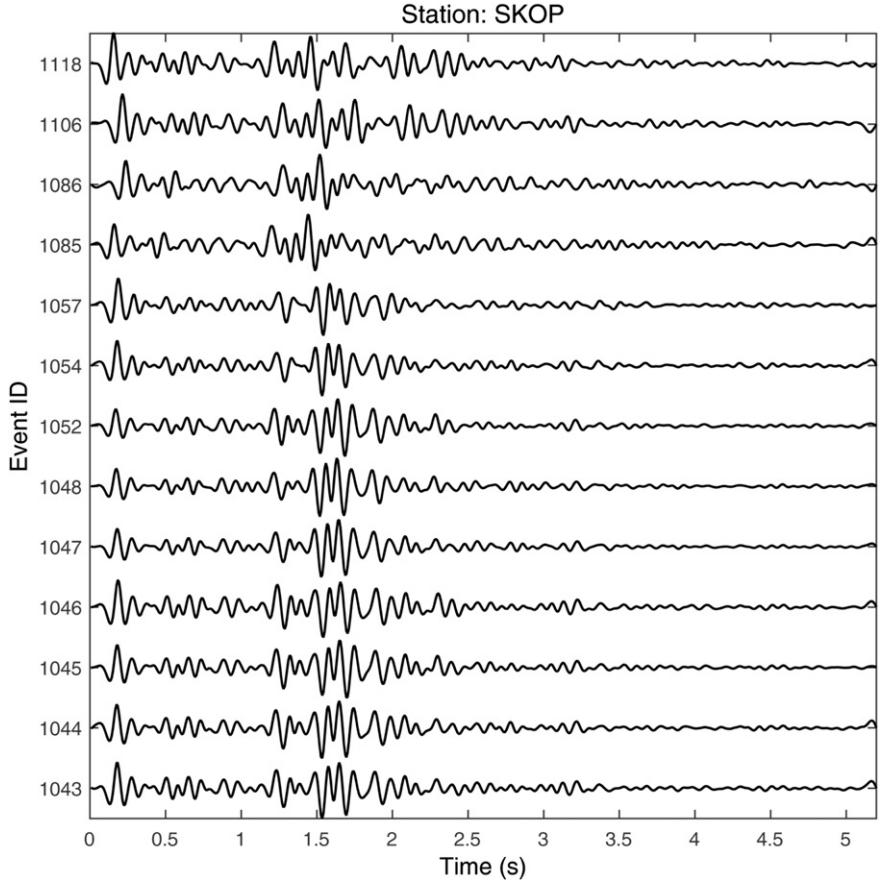


**Fig. 10.** Waveforms of the second multiplet recorded at station SKOP.

pattern provides evidence for a possible source below the depth of 4 km, which initiates the seismicity and then migrates to shallower depths, most probably to meet the surface.

The interevent times of the earthquakes located in the southern cluster are examined in order to find whether they occurred as independent events (following a Poisson process) or are triggered by each other. The probability density function of different distributions (Lognormal, Weibul, Gamma, Exponential) is fitted to the observed interevent times. These distributions are widely discussed and used to describe the interevent time distribution in several studies. Particularly, the Exponential distribution (Poisson process) was used for describing induced seismicity during injections (Langenbruch et al., 2011), which means that only the fluid source is responsible for the generation of the earthquakes. In our study, Lognormal is chosen as the best model for the dataset, meaning that an earthquake - earthquake triggering process is mainly dominating the seismogenesis in the area.

Triggering mechanisms such as Coulomb stress changes, fluid intrusion and estimation of multiplet events are examined and discussed. Particularly, Coulomb stress changes calculated on a vertical plane after the occurrence of the $M_w = 4.1$ earthquake according to the faulting type of the southern cluster, show that the area is closer to failure. Almost all the events comprising the southern cluster are located in an area with positive stress changes and several of them in lobes with $\Delta CFF > 0.01$ MPa. In cases of earthquake swarms (e.g. Mesimeri et al., 2016) or in mining induced seismicity (e.g. Orlecka-Sikora, 2010) it has been addressed that earthquakes were triggered even in areas of $\Delta CFF > 0.005$ MPa. Thus, the values of ΔCFF are considered to be adequate for triggering new events in the area.

Focusing on the southern cluster, we searched for possible triggering due to fluid intrusion. The two noticeable periods were separately examined and revealed that the spatio-temporal earthquake occurrence could be described by a parabolic envelope curve. In addition to the triggering front, which is a signature of hydraulically triggered seismicity (Shapiro, 2015), a back front was observed which explains the occurrence of earthquakes after the stop of the fluid intrusion (Parotidis et al., 2004). Multiplets of repeating events, which are searched over the full waveform, reveal that certain patches ruptured especially in the southern part, where a major multiplet consisting of 661 events was found. Waveform similarity and the similar locations of the events comprised in the multiplets are evidence that a same mechanism was responsible for earthquake triggering.

All the above constitute evidence for a possible fluid source in the area, which is mostly responsible for the initiation of the microseismic activity. The fluid source is most probably CO2, which is found in several sites throughout the Florina Basin (Koukouzas et al., 2015). Similar cases are addressed in the literature (e.g. Fischer et al., 2014) and a clear relation between microseismicity and episodes of $CO_2$ degassing is found. However, the case of Florina Basin is different due to lack of dense seismicity monitoring. This kind of seismicity is first observed by the deployment of the local network and associated with the $CO_2$ emissions that occurred in the area. Thus, future work should be focused on the permanent monitoring of the seismicity in the area along with observations by other scientific fields (e.g. geochemistry, tectonics etc.).

Concluding, we suggest that the southern part of the study area was in a near failure state after the $M_w = 4.1$ earthquake on 17 February 2013 due to stress transfer. $CO_2$ emissions used nearby fault segments as pathways, which were near failure due to this moderate event, and initiated the seismicity burst in the area. The interevent time distribution of the events on the southern cluster reveals that the earthquakes are not occurring independently, but they are triggered by each other.

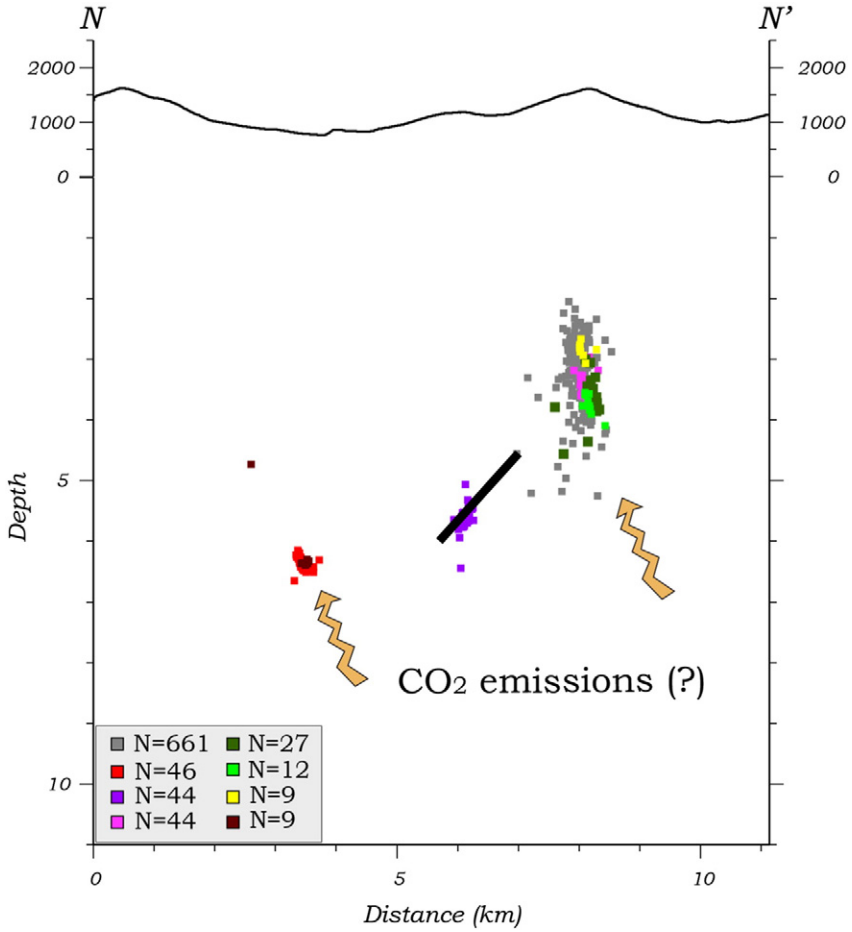


**Fig. 11.** Cross section (N-N′ in Fig. 3) of the foci of the repeating events along with the fault plane (black line) associated with the major event ($M_w = 4.1$).

However, the analysis of depth distribution shows that the influence of fluids is considerable. Diffusion curves verify the fluid induced seismicity in most cases, whereas repeating events showed that the mechanism rupturing the main southern cluster is the same. These findings led us to the conclusion that microseismicity in the area is occurring as a combination of fluid intrusion and earthquake - earthquake triggering.

## Acknowledgements

The authors appreciate the editorial assistance of Dr. Wang and the constructive comments of the two anonymous reviewers, which contributed to the improvement of the manuscript. The software Generic Mapping Tools was used to plot some figures (Wessel and Smith, 1998). The stress tensors were calculated using a program written by J. Deng (Deng and Sykes, 1997), based on the DIS3D code of S. Dunbar, which later improved (Erickson, 1986) and the expressions of G. Converse. V.K., E.P. and T.T. express their sincere thanks to the Region of Western Macedonia and Regional Unity of Florina for the financial support of the present study through the research project 'Study of seismic activity in the area of Florina'. Geophysics Department Contribution 864.

## References

Aki, K., 1965. Maximum likelihood estimate of b in the formula logN = a-bM and its confidence limits. Bull. Earthq. Res. Inst. 237–239.
Aki, K., Richards, P.G., 2002. Quantitative Seismology. second ed. University Science Books.
Bak, P., Christensen, K., Danon, L., Scanlon, T., 2002. Unified scaling law for earthquakes. Phys. Rev. Lett. 88:10–13. http://dx.doi.org/10.1103/PhysRevLett.88.178501.
Brune, J.N., 1970. Tectonic stress and the spectra of seismic shear waves from earthquakes. J. Geophys. Res. 75:4997. http://dx.doi.org/10.1029/JB075i026p04997.
Corral, A., 2004. Long-term clustering, scaling, and universality in the temporal occurrence of earthquakes. Phys. Rev. Lett. 92:1–4. http://dx.doi.org/10.1103/PhysRevLett.92.108501.
Corral, A., 2006. Dependence of earthquake recurrence times and independence of magnitudes on seismicity history. Tectonophysics 424:177–193. http://dx.doi.org/10.1016/j.tecto.2006.03.035.
Davidsen, J., Kwiatek, G., 2013. Earthquake interevent time distribution for induced micro-, nano-, and picoseismicity. Phys. Rev. Lett. 110:1–5. http://dx.doi.org/10.1103/PhysRevLett.110.068501.
Deng, J., Sykes, L.R., 1997. Evolution of the stress field in southern California and triggering of moderate-size earthquakes: a 200-year perspective. J. Geophys. Res. 102, 9859–9886.
Drakatos, G., Voulgaris, N., Pirli, M., Melis, N., Karakostas, B., 2005. 3-D crustal velocity structure in northwestern Greece. Pure Appl. Geophys. 162:37–51. http://dx.doi.org/10.1007/s00024-004-2578-2.
Erickson, L., 1986. User's Manual for DIS3D: A Three Dimensional Dislocation Program With Applications to Faulting in the Earth. Master's Thesis. Stanford University, p. 167.
Fischer, T., Horálek, J., Hrubcová, P., Vavryčuk, V., Bräuer, K., Kämpf, H., 2014. Intra-continental earthquake swarms in West-Bohemia and Vogtland: a review. Tectonophysics 611:1–27. http://dx.doi.org/10.1016/j.tecto.2013.11.001.
Godano, C., 2015. A new expression for the earthquake interevent time distribution. Geophys. J. Int. 202:219–223. http://dx.doi.org/10.1093/gji/ggv135.
Got, J.-L., Fréchet, J., Klein, F.W., 1994. Deep fault plane geometry inferred from multiplet relative relocation beneath the south flank of Kilauea. J. Geophys. Res. 99: 15375–15386. http://dx.doi.org/10.1029/94JB00577.
Hainzl, S., 2004. Seismicity patterns of earthquake swarms due to fluid intrusion and stress triggering. Geophys. J. Int. 159:1090–1096. http://dx.doi.org/10.1111/j.1365-246X.2004.02463.x.
Hainzl, S., Fischer, T., 2002. Indications for a successively triggered rupture growth underlying the 2000 earthquake swarm in Vogtland/NW Bohemia. J. Geophys. Res. 107: 1–9. http://dx.doi.org/10.1029/2002JB001865.
Hainzl, S., Fischer, T., Dahm, T., 2012. Seismicity-based estimation of the driving fluid pressure in the case of swarm activity in Western Bohemia. Geophys. J. Int. 191: 271–281. http://dx.doi.org/10.1111/j.1365-246X.2012.05610.x.
Hanks, T.C., Kanamori, H., 1979. A moment magnitude scale. J. Geophys. Res. 84, 2348–2350.
Harris, R.A., 1998. Introduction to special section: stress triggers, stress shadows, and implications for seismic hazard. J. Geophys. Res. B Solid Earth 103, 24347–24358.
Hatzfeld, D., Christodoulou, A.A., Scordilis, E.M., Panagiotopoulos, D., Hatzidimitriou, P.M., 1987. A microearthquake study of the Mygdonian Graben (Northern Greece). Earth Planet. Sci. Lett. 81, 379–396.
Hatzfeld, D., Karakostas, V., Ziazia, M., Selvaggi, G., Leborgne, S., Berge, C., Makropoulos, K., 1997. The Kozani-Grevena (Greece) earthquake of 13 May 1995 revisited from a detailed seismological study. Bull. Seismol. Soc. Am. 87, 463–473.
Hatziyannis, G., 2007. The role of capture and storage of $CO_2$ (C.C.S. - capture and storage of $CO_2$) when dealing with climate change. IENE Conference on Climate Change, Athens, Greece.
Karakostas, V.G., Papadimitriou, E.E., Karakaisis, G.F., Papazachos, C.B., Scordilis, E.M., Vargemezis, G., Aidona, E., 2003. The 2001 Skyros, Northern Aegean, Greece, earthquake sequence: off - fault aftershocks, tectonic implications, and seismicity triggering. Geophys. Res. Lett. 30:10–13. http://dx.doi.org/10.1029/2002GL015814.
Karakostas, V.G., Papadimitriou, E.E., Papazachos, C.B., 2004. Properties of the 2003 Lefkada, Ionian Islands, Greece, earthquake seismic sequence and seismicity triggering. Bull. Seismol. Soc. Am. 94:1976–1981. http://dx.doi.org/10.1785/012003254.
Karakostas, V., Papadimitriou, E., Gospodinov, D., 2014. Modelling the 2013 North Aegean (Greece) seismic sequence: geometrical and frictional constraints, and aftershock probabilities. Geophys. J. Int. 197, 525–541.
Kissling, E., Ellsworth, W.L., Kradolfer, U., 1994. Initial reference models in local earthquake tomography. J. Geophys. Res. 99, 19,635–19,646.
Klein, F.W., 2002. User's Guide to HYPOINVERSE-2000, A Fortran Program to Solve Earthquakes Locations and Magnitudes. U.S Geological Survey Open File Report 02-171 (version 1.0).
Koukouzas, N., Tasianas, A., Gemeni, V., Alexopoulos, D., Vasilatos, C., 2015. Geological modelling for investigating $CO_2$ emissions in Florina basin. Greece. Open Geosci. 7: 465–489. http://dx.doi.org/10.1515/geo-2015-0039.
Langenbruch, C., Dinske, C., Shapiro, S.A., 2011. Inter event times of fluid induced earthquakes suggest their Poisson nature. Geophys. Res. Lett. 38:1–6. http://dx.doi.org/10.1029/2011GL049474.
Mayr, S.I., Stanchits, S., Langenbruch, C., Dresen, G., Shapiro, S.A., 2011. Acoustic emission induced by pore-pressure changes in sandstone samples. Geophysics 76, MA21–MA32.
Mesimeri, M., Karakostas, V., Papadimitriou, E., Schaff, D., Tsaklidis, G., 2016. Spatio-temporal properties and evolution of the 2013 Aigion earthquake swarm (Corinth Gulf, Greece). J. Seismol. 20:595–614. http://dx.doi.org/10.1007/s10950-015-9546-4.
Miller, S.A., Collettini, C., Chiaraluce, L., Cocco, M., Barchi, M., Kaus, B.J.P., 2004. Aftershocks driven by a high-pressure $CO_2$ source at depth. Nature 427:724–727. http://dx.doi.org/10.1038/nature02251.
Orlecka-Sikora, B., 2010. The role of static stress transfer in mining induced seismic events occurrence, a case study of the Rudna mine in the Legnica-Glogow Copper District in Poland. Geophys. J. Int. 182:1087–1095. http://dx.doi.org/10.1111/j.1365-246X.2010.04672.x.
Paige, C., Saunders, M., 1982. LSQR: an algorithm for sparse linear equations and sparse least squares. ACM Trans. Math. Softw. 8, 43–71.
Panagiotopoulos, D.G., Papazachos, B.C., 1985. Travel times of Pn -waves in the Aegean and surrounding area. Geophys. J. R. Astron. Soc. 80, 165–176.
Papadimitriou, E., Karakostas, V., Mesimeri, M., Vallianatos, F., 2016. The Mw 6.7 12 October 2013 western Hellenic Arc main shock and its aftershock sequence: implications for the slab properties. Int. J. Earth Sci. http://dx.doi.org/10.1007/s00531-016-1294-3.
Papazachos, B.C., Papazachou, C., 2003. The Earthquakes of Greece. Ziti publications, Thessaloniki.
Papazachos, B.C., Scordilis, E.M., Panagiotopoulos, D.G., Papazachos, C.B., Karakaisis, G.F., 2004. Global relations between seismic fault parameters and moment magnitudes of earthquakes. Bull. Geol. Soc. Greece, XXXVI.
Papazachos, B.C., Papadimitriou, E.E., Kiratzi, A.A., Papazachos, C.B., Louvari, E.K., 1998. Fault plane solutions in the Aegean Sea and the surrounding area and their tectonic implication. Boll. Geofis. Teor. Appl. 39, 199–218.
Parotidis, M., Rothert, E., Shapiro, S.A., 2003. Pore-pressure diffusion: a possible triggering mechanism for the earthquake swarms 2000 in Vogtland/NW-Bohemia, central Europe. Geophys. Res. Lett. 30:10–13. http://dx.doi.org/10.1029/2003GL018110.
Parotidis, M., Shapiro, S.A., Rothert, E., 2004. Back front of seismicity induced after termination of borehole fluid injection. Geophys. Res. Lett. 31:1–5. http://dx.doi.org/10.1029/2003GL018987.
Parotidis, M., Shapiro, S.A., Rothert, E., 2005. Evidence for triggering of the Vogtland swarms 2000 by pore pressure diffusion. J. Geophys. Res. B Solid Earth 110:1–12. http://dx.doi.org/10.1029/2004JB003267.
Rice, J.R., Cleary, M.P., 1976. Some basic stress diffusion solutions for fluid-saturated elastic porous media with compressible constituents. Rev. Geophys. 14, 227–241.
Robinson, R., McGinty, P.J., 2000. The enigma of the Arthur's Pass, New Zealand, earthquake: 2. The aftershock distribution and its relation to regional and induced stress fields. J. Geophys. Res. 105:16139. http://dx.doi.org/10.1029/2000JB900012.
Schaff, D.P., Richards, P.G., 2004. Repeating seismic events in China. Science 303 (80), 1176–1179.
Schaff, D.P., Richards, P.G., 2011. On finding and using repeating seismic events in and near China. J. Geophys. Res. Solid Earth 116:1–20. http://dx.doi.org/10.1029/2010JB007895.
Schaff, D.P., Waldhauser, F., 2005. Waveform cross-correlation-based differential travel-time measurements at the northern California seismic network. Bull. Seismol. Soc. Am. 95, 2446–2461.
Schaff, D.P., Bokelmann, G.H.R., Ellsworth, W.L., Zanzerkia, E., Waldhauser, F., Beroza, G.C., 2004. Optimizing correlation techniques for improved earthquake location. Bull. Seismol. Soc. Am. 94, 705–721.
Shapiro, S.A., 2015. Fluid-Induced Seismicity. Cambridge University Press.
Shapiro, S.A., Huenges, E., Borm, G., 1997. Estimating the crust permeability from fluid-injection-induced seismic emission at the KTB site. Geophys. J. Int. 131:F15–F18. http://dx.doi.org/10.1111/j.1365-246X.1997.tb01215.x.
Shapiro, S.A., Rothert, E., Rath, V., Rindschwentner, J., 2002. Characterization of fluid transport properties of reservoirs using induced microseismicity. Geophysics 67:212. http://dx.doi.org/10.1190/1.1451597.
Shelly, D.R., Hill, D.P., Massin, F., Farrell, J., Smith, R.B., Taira, T., 2013. A fluid-driven earthquake swarm on the margin of the Yellowstone caldera. J. Geophys. Res. E Planets 118:4872–4886. http://dx.doi.org/10.1002/jgrb.50362.

Sokos, E.N., Zahradnik, J., 2008. ISOLA a Fortran code and a Matlab GUI to perform multiple-point source inversion of seismic data. Comput. Geosci. 34:967–977. http://dx.doi.org/10.1016/j.cageo.2007.07.005.

Sokos, E.N., Zahradnik, J., 2013. Evaluating centroid-moment-tensor uncertainty in the new version of ISOLA software. Seismol. Res. Lett. 84:656–665. http://dx.doi.org/10.1785/0220130002.

Stanchits, S., Mayr, S., Shapiro, S., Dresen, G., 2011. Fracturing of porous rock induced by fluid injection. Tectonophysics 503:129–145. http://dx.doi.org/10.1016/j.tecto.2010.09.022.

Stein, R.S., 1999. The role of stress transfer in earthquake occurrence. Nature 402: 605–609. http://dx.doi.org/10.1038/45144.

Stein, R.S., King, G.C.P., Lin, J., 1994. Stress triggering of the 1994 M = 6.7 Northridge, California, earthquake by its predecessors. Science 265 (80), 1432–1435.

Touati, S., Naylor, M., Main, I.G., 2009. Origin and nonuniversality of the earthquake interevent time distribution. Phys. Rev. Lett. 102:1–4. http://dx.doi.org/10.1103/PhysRevLett.102.168501.

Touati, S., Naylor, M., Main, I.G., Christie, M., 2011. Masking of earthquake triggering behavior by a high background rate and implications for epidemic-type aftershock sequence inversions. J. Geophys. Res. Solid Earth 116:1–16. http://dx.doi.org/10.1029/2010JB007544.

Valoroso, L., Chiaraluce, L., Piccinini, D., Di Stefano, R., Schaff, D., Waldhauser, F., 2013. Radiography of a normal fault system by 64,000 high-precision earthquake locations: the 2009 L'Aquila (central Italy) case study. J. Geophys. Res. Solid Earth 118: 1156–1176. http://dx.doi.org/10.1002/jgrb.50130.

Waldhauser, F., 2001. HypoDD - A Program to Compute Double-difference Hypocenter Locations (01-113).

Waldhauser, F., Ellsworth, W.L., 2000. A double-difference earthquake location algorithm: method and application to the northern Hayward fault, California. Bull. Seismol. Soc. Am. 90:1353–1368. http://dx.doi.org/10.1785/0120000006.

Waldhauser, F., Schaff, D.P., 2008. Large-scale relocation of two decades of Northern California seismicity using cross-correlation and double-difference methods. J. Geophys. Res. Solid Earth 113:1–15. http://dx.doi.org/10.1029/2007JB005479.

Wells, D.L., Coppersmith, K.J., 1994. New empirical relationships among magnitude, rupture length, rupture width, rupture area, and surface displacement. Bull. Seismol. Soc. Am. 84, 974–1002.

Wessel, P., Smith, W.H.F., 1998. New, improved version of the generic mapping tools released. EOS Trans. Am. Geophys. Union 79, 579.

Wiemer, S., Wyss, M., 2000. Minimum magnitude of completeness in earthquake catalogs: examples from Alaska, the Western United States, and Japan. Bull. Seismol. Soc. Am. 90:859–869. http://dx.doi.org/10.1785/0119990114.

Ziogou, E., Germeni, V., Koukouzas, N., de Angelis, D., Libertini, S., Beaubien, S.E., Lombardi, S., West, J.M., Jones, D.G., Coombs, P., Barlow, T., Gwosdz, S., Kruger, M., 2013. Potential environmental impacts of CO2 leakage from the study of natural analogue sites in Europe. Eur. Energy Procedia 37, 1–8.